Journal of Materials Research and Technology 43 (2026) 1676–1682

Contents lists available at ScienceDirect

Journal of Materials Research and Technology

journal homepage: www.elsevier.com/locate/jmrt

Evolution of time-dependent deformation in a Ti-rich Ti–Ni–Cu–Pd alloy from solution-treated to aged states: Insights from spherical nanoindentation

Hang Li [a,b,*], Zhe Gao [c], Xingxing Bai [d], Yongming Jin [d], Xianglong Meng [e], Wei Cai [e], Jae-il Jang [c]

[a] School of Energy and Materials, Shihezi University, Shihezi, 832000, China
[b] Institute of Bingtuan Energy Development Research, Shihezi University, Shihezi, 832000, China
[c] Division of Materials Science and Engineering, Hanyang University, Seoul, 04763, Republic of Korea
[d] Analysis and Testing Center, Xinjiang University, Urumqi, China
[e] School of Materials Science and Engineering, Harbin Institute of Technology, Harbin, 150006, China

ARTICLE INFO

Keywords:
Shape memory alloys
Ti–Ni–Cu–Pd alloy
Creep
Nanoindentation

ABSTRACT

The time-dependent plastic deformation behavior of the Ti-rich Ti–Ni–Cu–Pd alloy in solution-treated and aged states was systematically investigated through spherical nanoindentation creep experiments. The indentation creep results reveal that appreciable creep deformation occurs in both solution-treated and aged states even at room temperature, whereas the creep deformation in the aged state is significantly less pronounced than that in the solution-treated state. The dominant creep mechanisms in the two states are discussed on the basis of the obtained values of the creep stress exponent, *n*, and the corresponding activation volumes.

1. Introduction

Shape memory alloys (SMAs) are functional metallic materials capable of producing large recoverable deformation through reversible martensitic transformation, enabling integrated actuation and sensing without complex mechanical systems [1,2]. Among them, Ti–Ni-based alloys are the most widely used commercial SMAs owing to their excellent recoverability and mechanical reliability. However, conventional Ti–Ni alloys usually exhibit a relatively large transformation hysteresis of approximately 25-40 °C, which limits their actuation sensitivity, response speed, and energy efficiency. Moreover, functional degradation during repeated thermal or mechanical cycling, including transformation temperature shifts, residual strain accumulation, and reduced cyclic stability, remains a major obstacle to their long-term application [3–5]. The geometrically nonlinear theory of martensite (GNLTM) suggests that low-hysteresis transformation can be achieved by bringing the middle eigenvalue λ_2 close to unity [6]. Following this criterion, our previous work designed off-stoichiometric Ti–Ni–Cu–Pd alloys through Pd-mediated lattice-parameter tuning, leading to ultra-narrow hysteresis, transformation-temperature variation below 1 °C after 5000 thermal cycles, and suppressed defect accumulation during cycling [7–9]. The resulting defect-resistant transformation further enabled reproducible temperature memory behavior and stable shape recovery with narrow stress-assisted hysteresis under external loading [10,11].

Although Ti–Ni–Cu–Pd alloys have shown ultra-narrow transformation hysteresis and excellent cyclic stability, these advantages mainly reflect their transformation reversibility under thermal or cyclic loading conditions. For practical SMA actuators, however, long-term dimensional stability also depends on the resistance to time-dependent deformation under sustained or localized mechanical loading, since structural and functional fatigue remain critical factors limiting the service life of SMA components [12,13]. During service, bias stress, contact stress, clamping, or mechanical constraint may induce creep-like deformation at room temperature, leading to residual deformation accumulation and reduced actuation precision [14]. Therefore, the room-temperature time-dependent deformation behavior of Ti–Ni–Cu–Pd alloys needs to be further clarified. A comparison between the solution-treated and aged states provides an effective way to examine how aging-modulated microstructures influence this deformation behavior, because aging-induced precipitation and internal microstructural changes have been shown to strongly affect the functional

---

[*] Corresponding author. School of Energy and Materials, Shihezi University, Shihezi, 832000, China.
E-mail address: lihanglihang2002@163.com (H. Li).

https://doi.org/10.1016/j.jmrt.2026.06.197
Received 15 May 2026; Received in revised form 19 June 2026; Accepted 20 June 2026

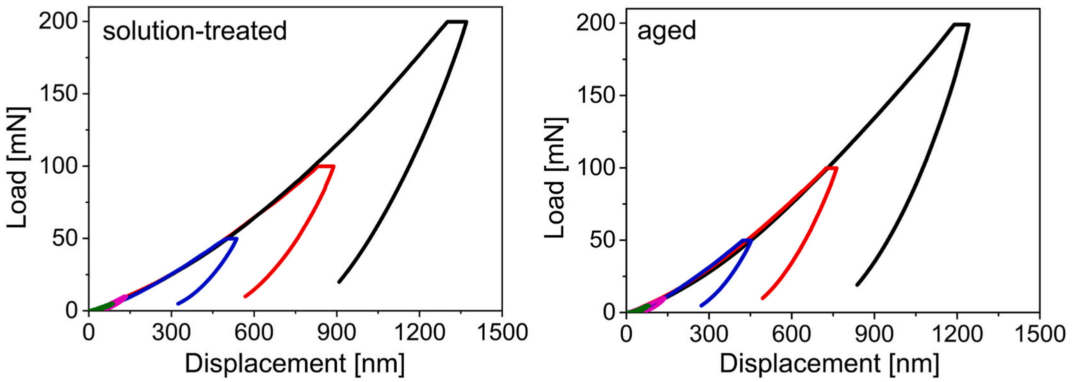

Fig. 1. Representative load–displacement curves recorded during spherical indentation creep experiments in (a) the solution-treated state and (b) the aged state.

stability of TiNiPdCu-based alloys [15,16]. The solution-treated alloy represents a relatively weakly strengthened matrix, whereas aging treatment may induce solute redistribution, defect rearrangement, precipitation strengthening, and internal stress fields. These microstructural changes are expected to affect the local deformation resistance and the accumulation of unrecovered displacement during sustained loading. Thus, investigating the creep response of solution-treated and aged Ti-rich Ti–Ni–Cu–Pd alloys is important for evaluating whether aging treatment can enhance their resistance to room-temperature time-dependent deformation. Nanoindentation creep testing is particularly suitable for this Pd-containing alloy system. Our previous work has demonstrated that spherical nanoindentation is capable of probing the local transformation-related mechanical response of Ti–Ni-based SMAs, particularly the superelastic deformation behavior under localized contact loading [17,18]. Building on this methodological basis, nanoindentation creep testing provides a further opportunity to evaluate the time-dependent deformation stability of Ti-rich Ti–Ni–Cu–Pd alloys under sustained local stress. On the one hand, nanoindentation probes the creep response under a highly localized contact stress field, which is relevant to the local contact, clamping, and constraint conditions experienced by SMA components in service. On the other hand, it requires only a small material volume, which is advantageous for Ti–Ni–Cu–Pd alloys because Pd-containing SMA systems involve expensive noble-metal additions, making large-sized specimens costly to prepare [19]. By monitoring the penetration-depth evolution during the constant-load holding stage, nanoindentation enables sensitive evaluation of room-temperature creep displacement, creep strain-rate evolution, and local deformation stability; in this context, a spherical indenter is more suitable than a Berkovich indenter [20–26]. Accordingly, this study investigates the spherical nanoindentation creep behavior of solution-treated and aged Ti-rich Ti–Ni–Cu–Pd alloys to clarify the effect of aging on local time-dependent deformation and room-temperature creep resistance.

2. Experimental procedures

A Ti-rich Ti$_{50.5}$Ni$_{33.5}$Cu$_{11.5}$Pd$_{4.5}$ alloy (at.%) was used in this study. Two material states were prepared for comparison: the solution-treated state and the aged state. The solution-treated samples were produced by annealing at 950 °C for 2 h, and the aged samples were subsequently obtained by aging the solution-treated specimens at 500 °C for 1 h. As reported in our previous work [27], the aged specimen contains fine, uniformly dispersed nanoscale precipitates with characteristic sizes of approximately 5-20 nm. These precipitates were identified as a Ti$_2$Cu-type phase with a tetragonal C11b structure, with an estimated volume fraction of approximately 7-10 vol%. Room-temperature nanoindentation creep tests were carried out using a Nanoindenter XP system (KLA) equipped with a spherical diamond tip. The effective indenter radius was 34.9 μm, as calibrated from Hertzian analysis of reference indentations performed on fused quartz. Prior to testing, all specimen surfaces were carefully vibration-polished using 0.02 μm colloidal silica suspension to minimize surface-roughness effects. During each indentation test, the load was increased to a prescribed maximum load, $P_{\max}$, at a constant loading rate of 0.5 mNs^{-1}. The load was then maintained at $P_{\max}$ for 1000 s to record the time-dependent displacement response, followed by complete unloading. For each material condition, more than ten independent indents were performed to ensure the reproducibility of the measured creep response.

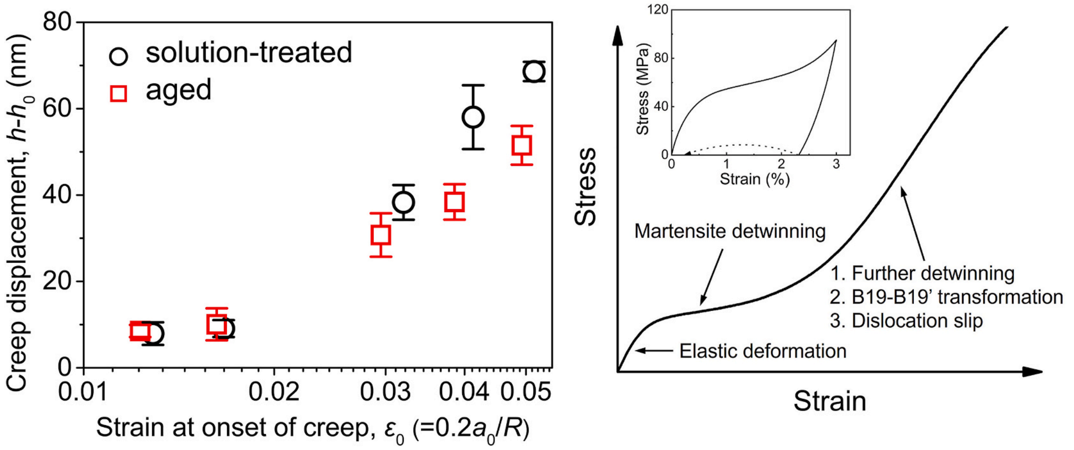

Fig. 2. (A) Schematic illustration of the deformation mechanism and recovery behavior after 3% deformation [27] of the solution-treated Ti–Ni–Cu–Pd alloy in the martensitic state. (b) Dependence of creep displacement on strain at the onset of creep in the solution-treated and aged states.

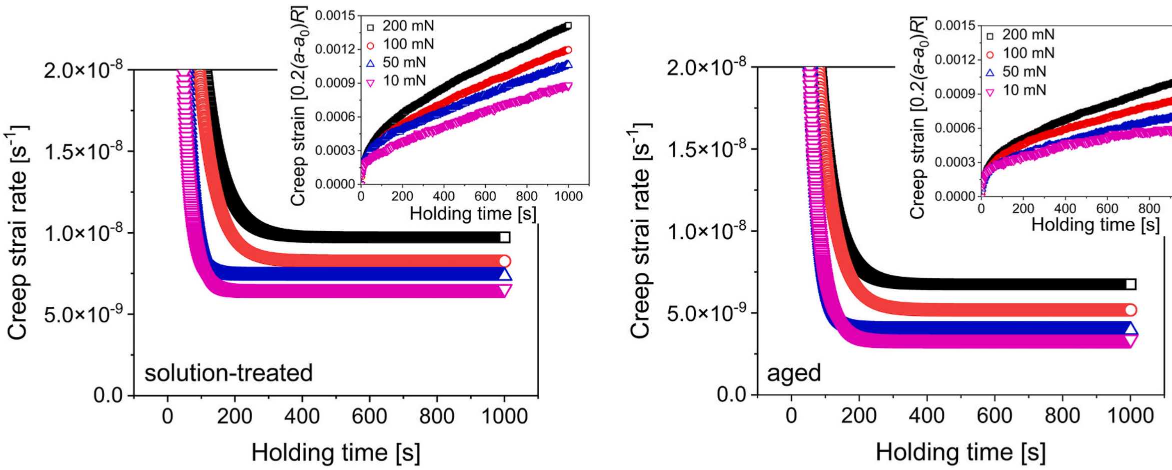

Fig. 3. Representative evolution of strain rate with holding time, with the inset showing creep strain as a function of holding time; (a) the solution-treated state and (b) the aged state.

3. Results and discussion

Representative load–displacement responses obtained from spherical indentation creep tests are provided in Fig. 1. For comparison, the curves corresponding to the solution-treated condition and the aged sample are displayed separately, revealing the influence of aging treatment on the indentation response. For both conditions, as the peak load increased gradually from 10 to 200 mN, the maximum penetration depth increased markedly, indicating an enlarged stressed volume beneath the spherical indenter and a progressively enhanced degree of local deformation. At each peak load, the indentation depth continued to increase during the constant-load holding segment, demonstrating a pronounced time-dependent deformation behavior at room temperature. At relatively low loads, the increase in indentation depth during holding suggests that creep deformation can occur even when the local deformation has not yet developed into macroscopic yielding. Since the alloy is in the martensitic state at the testing temperature, the holding-induced displacement increase should not be simply attributed to ordinary elastic hysteresis or viscoelastic-like response.

To further clarify the physical deformation processes that may correspond to the above-mentioned displacement increase during the holding stage, Fig. 2a presents a schematic illustration of the deformation mechanism of the solution-treated Ti–Ni–Cu–Pd alloy in the martensitic state, together with its recovery behavior after deformation to 3% [27]. The deformation result provides a necessary deformation-path reference for the subsequent analysis of the nanoindentation creep mechanism. As shown in Fig. 2a, at the initial loading stage, the alloy mainly undergoes elastic deformation of the martensitic matrix, and the stress increases approximately linearly with strain. With further increasing strain, the slope of the curve decreases, indicating that the deformation enters a stage dominated by martensite detwinning. During this stage, the applied stress drives the growth of favorably oriented martensite variants, accompanied by twin-boundary migration, thereby producing a large recoverable deformation. When the strain continues to increase, simple martensite detwinning gradually tends to become saturated, and further deformation needs to be accommodated by continued detwinning, stress-assisted B19→B19’ martensite-to-martensite transformation, and local dislocation slip. Unlike NiTi-based SMAs with an initial B19’ martensitic structure, the alloy investigated in this study mainly consists of B19 martensite in the unloaded state. Therefore, in addition to driving martensite variant rearrangement and detwinning, the applied stress may also induce the B19→B19’ martensite-to-martensite transformation [28], whereas the deformation of the former usually does not involve such a B19→B19’ transformation process. At this stage, the deformation process is no longer completely governed by reversible interface motion, but may also be accompanied by local irreversible plastic deformation. The inset in Fig. 2a shows that, after the solution-treated sample was deformed to 3%, it could not fully recover to its initial state even after unloading and subsequent heating, indicating that an incompletely recoverable deformation component had already been introduced at this strain level. This result suggests that, in the deformation range of approximately 3% and above, martensite detwinning are insufficient to fully accommodate the applied deformation, and B19→B19’ transformation-interface migration and local dislocation slip begin to participate in the deformation process. Therefore, in the subsequent nanoindentation creep analysis, the displacement increases during the holding stage within the indentation strain range of 3%–5% should not be simply interpreted as elastic hysteresis or a single interface-motion process, but rather as the combined result of continued martensitic interface migration, local transformation accommodation, and irreversible plastic deformation.

The variation in creep displacement with the strain at the onset of creep is summarized in Fig. 2b. The total creep displacement, h_{creep}, is defined as the maximum value of h–h_0 at 1000 s, where the subscript 0 denotes the onset of creep in the following discussion. For spherical indentation, the indentation strain, ε_i, is commonly expressed as $0.2a/R_i$, where a represents the radius of the contact area and R_i denotes the spherical indenter radius [29]. It can be observed that, for both conditions, the creep displacement increases with increasing initial indentation strain. This indicates that a higher indentation strain enhances the local stress concentration and martensitic structural adjustment beneath the indenter, thereby promoting further interface migration and irreversible deformation during the holding stage. In the lower strain range, the difference in creep displacement between the solution-treated and aged samples is relatively small, suggesting that the deformation beneath the indenter is mainly accommodated by the elastic response of martensite and initial variant rearrangement, while the suppressing effect of precipitates on creep displacement is not yet pronounced. When the indentation strain increases to approximately 3%–5%, the creep displacement of the aged sample becomes markedly lower than that of the solution-treated sample, indicating that fine dispersed precipitates [27] exert a stronger inhibitory effect on martensite detwinning, the B19 → B19’ transformation, and local dislocation slip under higher strain conditions.

To further characterize the time-dependent deformation behavior, the evolution of strain rate during the holding stage was analyzed, as shown in Fig. 3. The corresponding creep strain–time curves are included in the insets, allowing the creep response of the solution-treated and aged samples to be compared over the holding period. To quantitatively evaluate the indentation creep response, the indentation

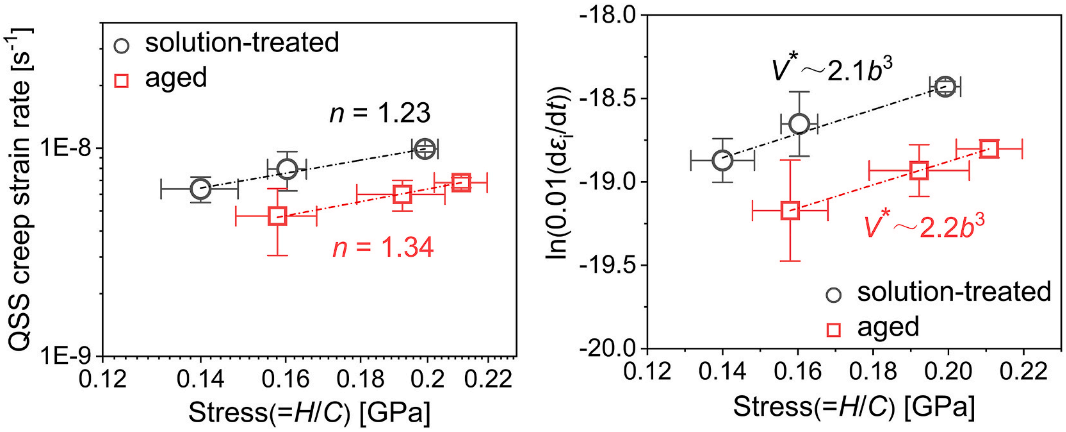

Fig. 4. (A) Quasi-steady-state creep strain rate as a function of stress, where the slope yields the creep stress exponent n. (b) Stress dependence of the logarithmic creep strain rate for estimating the activation volume V^*.

creep strain, $\varepsilon_{\text{creep}}$, was determined from the variation in contact radius during the load-holding stage. For spherical indentation, it can be expressed as

$$\varepsilon_{\text{creep}} = \varepsilon_i - (\varepsilon_i)_0 = \frac{0.2(a - a_0)}{R} \tag{1}$$

where a_0 and a denote the contact radii at the beginning of creep and at a given holding time, respectively, and R is the radius of the spherical indenter. According to the geometrical relationship for spherical contact, the contact radius was approximated by [30]

$$a = \left(2hR - h^2\right)^{1/2} \tag{2}$$

In the present analysis, the experimentally recorded indentation depth, h, was adopted for this calculation instead of the exact contact depth, h_c, in order to simplify the treatment. The calculated $\varepsilon_{\text{creep}}$ values for the solution-treated and aged samples are presented as a function of holding time, t_{hold}, in the insets of Fig. 3. The resulting $\varepsilon_{\text{creep}}$–$t_{\text{hold}}$ curves display a typical decelerating creep feature at the early stage, followed by a region with a much lower and nearly stabilized creep rate, resembling the transient-to-steady-state transition commonly observed in conventional high-temperature creep tests. To obtain the indentation strain rate, $\dot{\varepsilon}_i$, the $\varepsilon_{\text{creep}}$–$t_{\text{hold}}$ data were fitted using Garofalo's empirical creep equation, which was originally formulated for uniaxial creep deformation:

$$\varepsilon_i - (\varepsilon_i)_0 = \varepsilon_{\text{creep}} = \alpha\left(1 - e^{-rt_{\text{hold}}}\right) + \omega t_{\text{hold}} \tag{3}$$

where α, ω, and r are fitting parameters associated with the creep response. By differentiating Eq. (3) with respect to t_{hold}, the time-dependent indentation strain rate can be obtained as

$$\dot{\varepsilon}_i = \alpha r e^{-rt_{\text{hold}}} + \omega \tag{4}$$

Using the empirical correlation between the uniaxial creep strain rate and the indentation strain rate, namely $\dot{\varepsilon}_u \sim 0.01\dot{\varepsilon}_i$ [31], the evolution of $\dot{\varepsilon}_u$ with holding time was further derived for both the solution-treated and aged samples, as shown in the main panels of Fig. 3. The gradual decrease in strain rate and its subsequent tendency toward an approximately constant value indicate that a quasi-steady-state creep stage can be reached during spherical indentation creep testing. For both conditions, the creep strain rate decreases rapidly during the initial stage of holding and then gradually approaches a relatively stable quasi-steady-state regime. This behavior suggests that a pronounced transient stress-relaxation process occurs beneath the indenter at the beginning of the holding segment, during which a large number of mobile martensite twin boundaries and variant interfaces rapidly adjust under the applied contact stress. With increasing holding time, the number of readily movable interfaces gradually decreases and the local structure tends to stabilize; consequently, the creep strain rate decreases and enters a quasi-steady-state stage. The continuous increase in creep strain with holding time, as shown in the insets, further confirms that martensitic Ti–Ni–Cu–Pd alloys exhibit significant time-dependent deformation at room temperature. A comparison between the solution-treated and aged conditions shows that the aged sample generally exhibits a lower creep strain rate than the solution-treated sample under the same load, together with a smaller accumulation of creep strain. This indicates that aging-induced precipitates not only reduce the total creep displacement during the holding stage, but also decrease the rate of creep deformation. This can be attributed to the pinning effect of the precipitates and their surrounding elastic stress fields on martensite twin boundaries, variant interfaces, and B19/B19' transformation interfaces, which changes interface migration from a relatively free propagation process into a more constrained pinning–depinning process. Meanwhile, at higher indentation strains, the precipitates can also hinder local dislocation slip, thereby reducing the development rate of local irreversible deformation.

Identifying the rate-controlling creep mechanism is important for interpreting the room-temperature indentation creep response of Ti–Ni–Cu–Pd alloys. The creep stress exponent, n, is commonly used as a mechanistic indicator and can be defined as

$$n = \frac{\partial \ln \dot{\varepsilon}_{ss}}{\partial \ln \sigma} \tag{5}$$

where $\dot{\varepsilon}_{ss}$ is the steady-state creep strain rate and σ represents the applied stress. In general, $n \approx 1$ is usually associated with diffusion-controlled creep, including Nabarro–Herring creep controlled by lattice diffusion and Coble creep controlled by grain-boundary diffusion. A value of $n \approx 2$ is often related to grain-boundary sliding, whereas higher values, typically in the range of $n = 3$–8, are commonly taken as evidence of dislocation-mediated creep [32,33]. In the present work, the creep stress exponent was extracted from the spherical indentation creep results using the relationship

$$n = \frac{\partial \ln \dot{\varepsilon}_{QSS}}{\partial \ln \sigma} \tag{6}$$

where $\dot{\varepsilon}_{QSS}$ denotes the quasi-steady-state creep strain rate. The value of $\dot{\varepsilon}_{QSS}$ was taken at $t_{\text{hold}} = 1000$ s. Meanwhile, the corresponding stress was estimated from the indentation hardness measured at the same holding time according to Tabor's empirical relation,

$\sigma \sim \frac{H}{C}$ (7)where C is the constraint factor, which is generally taken to be approximately 3 for metallic materials [29]. It should be noted that the local stress beneath the indenter is not strictly constant during a constant-load indentation creep test, because the contact area and indentation depth continue to evolve with holding time. Therefore, the stress estimated at $t_{\mathrm{hold}} = 1000$ s was used here as an effective stress for comparing the quasi-steady-state creep response. The quasi-steady-state creep strain rate was then plotted as a function of applied stress, as presented in Fig. 4. By linearly fitting the average data points in the double-logarithmic $\dot{\varepsilon}_{QSS}$–σ plots, the corresponding creep stress exponents were obtained from the slopes. For the solution-treated and aged samples, the *n* values were approximately 1.23 and 1.34, respectively. Both values are close to 1 and are much lower than the high stress exponents typically associated with dislocation-slip- or dislocation-climb-controlled creep. Therefore, the room-temperature nanoindentation creep of this alloy at indentation strains of 3%–5% should not be simply attributed to conventional dislocation-controlled power-law creep. A more reasonable interpretation is that the rate-controlling process during the holding stage is mainly governed by martensitic interface motion, including martensite variant rearrangement, detwinning, twin-boundary migration, and localized stress-assisted B19→B19' transformation. It is worth noting that the *n* value of the aged sample is slightly higher than that of the solution-treated sample. This change indicates that the creep strain rate becomes somewhat more sensitive to stress after aging, but it does not necessarily imply a fundamental change in the creep mechanism. Since the *n* value of the aged sample remains close to 1, the dominant mechanism is still considered to be a martensitic-interface-controlled deformation process with relatively low stress sensitivity. The slight increase in *n* can be attributed to the pinning effect of fine dispersed precipitates on martensite twin boundaries and transformation interfaces. Compared with the more readily activated interface migration in the solution-treated state, further detwinning and B19/B19' interface propagation in the aged state require a higher local contact stress as the driving force, resulting in a slightly higher apparent stress exponent.

Additional information on the rate-controlling process can be obtained by evaluating the apparent activation volume, V^*, which is expressed as

$$V^* = \sqrt{3}kT\left(\frac{\partial \ln \dot{\varepsilon}_{QSS}}{\partial \sigma}\right) \tag{8}$$

where *k* is Boltzmann's constant and *T* is the absolute temperature. The activation volume is often used to characterize the characteristic volume involved in thermally activated deformation. Previous studies have shown that V^* can differ greatly depending on the dominant rate-limiting mechanism [34]. For example, dislocation glide in fcc metals generally corresponds to relatively large activation volumes, typically on the order of $\sim 100b^3$–$1000b^3$, whereas diffusion-controlled processes through the lattice or along grain boundaries usually give much smaller values, approaching the order of $\sim b^3$ [35,36]. In the present work, V^* was estimated from the stress dependence of the logarithmic creep strain rate, as shown in Fig. 4b. The Burgers vector, *b*, used for normalization was estimated to be 2.879×10^{-10} m for the solution-treated sample and 2.824×10^{-10} m for the aged sample. These values were then used to express the calculated activation volumes in units of b^3, allowing a more direct comparison with typical rate-controlling deformation mechanisms. For the solution-treated and aged samples, the V^* values were approximately $2.1b^3$ and $2.2b^3$, respectively. Both values are very small, indicating that the elementary activation events controlling room-temperature indentation creep are highly localized. If creep were governed by long-range dislocation glide, dislocation climb, or the unlocking of large-scale dislocation entanglements, a much larger cooperative deformation volume would generally be expected. In contrast, the activation volume of approximately $2b^3$ obtained in this study is closer to localized interfacial rearrangement events involving only a few atomic volumes. Therefore, the V^* results further support a martensitic-interface-controlled mechanism, in which creep is mainly governed by localized twin-boundary migration, martensite variant-interface propagation, and short-range motion of B19/B19' transformation interfaces. The slight increase in V^* from $2.1b^3$ in the solution-treated sample to $2.2b^3$ in the aged sample suggests that the precipitates slightly increase the cooperative volume required for local thermally activated events. This variation is consistent with the slight increase in *n*, indicating that aging-induced precipitates enhance the resistance to interface migration and localized transformation. However, the difference between the two values is very small, and V^* remains at a low level of approximately $2b^3$. This suggests that aging treatment does not change the creep mechanism into a conventional dislocation-controlled process. Instead, it gives rise to a precipitate-modulated martensitic-interface-controlled creep mechanism.

Table 1
Statistical results for the stress exponent *n* and activation volume *V** of the solution-treated and aged specimens.

Parameter	Solution-treated	Aged	95% CI of difference	*p*-value
n	1.23 ± 0.15 (95% CI: 0.965–1.557)	1.34 ± 0.58 (95% CI: 0.406–2.047)	−1.064–1.284	0.854
*V** (b^3)	2.10 ± 0.26 b^3 (95% CI: 1.637–2.654 b^3)	2.20 ± 0.99 b^3 (95% CI: 0.925–2.980 b^3)	−1.906–2.106 b^3	0.922

Note: Data are reported as the original fit estimate ± bootstrap standard deviation; CI denotes the 95% confidence interval.

Because the stress exponent *n* and activation volume *V** are regression-derived parameters obtained from the relationships between stress and quasi-steady-state creep strain rate at multiple load levels, rather than quantities measured directly from an individual indentation, a stratified nonparametric bootstrap procedure was used to quantify their fitting uncertainties. For each material condition, the independent indentation measurements were resampled with replacement within each load level. The mean stress and mean quasi-steady-state creep strain rate at each load level were then recalculated, and *n* and *V** were refitted. This procedure was repeated 10,000 times. To maintain consistency with the original regression analysis, the original fit values reported in Fig. 4 were retained as the parameter point estimates: $n = 1.23$ and 1.34 for the solution-treated and aged conditions, respectively, and $V^* = 2.1$ and 2.2 b^3, respectively. The bootstrap distributions were centered on these original regression estimates so that resampling was used only to quantify uncertainty. The parameters are reported as the original fit estimate ± bootstrap standard deviation, together with percentile-based 95% confidence intervals. Statistical significance was assessed using a two-sided bootstrap test based on the distribution of the aged-minus-solution-treated differences. The corresponding statistical results are summarized in Table 1.

The stress exponents were 1.23 ± 0.15 for the solution-treated specimen and 1.34 ± 0.58 for the aged specimen, with corresponding 95% confidence intervals of 0.965–1.557 and 0.406–2.047, respectively. Although *n* increased slightly from 1.23 to 1.34 after aging, the difference was not statistically significant ($p = 0.854$). The 95% confidence interval for the aged-minus-solution-treated difference was −1.064–1.284 and included zero. The corresponding activation volumes were 2.10 ± 0.26 b^3 and 2.20 ± 0.99 b^3, with 95% confidence intervals of 1.637–2.654 b^3 and 0.925–2.980 b^3, respectively. The increase in *V** from 2.1 to 2.2 b^3 was also not statistically significant ($p = 0.922$). The 95% confidence interval for the difference was −1.906–2.106 b^3 and likewise included zero. These statistical results show that aging produces only slight numerical increases in *n* and *V**, neither of which reaches statistical significance at the 0.05 level. More importantly, *n* remains within the same low-stress-exponent regime for both conditions, while *V** remains on the scale of only a few b^3. The results therefore support the conclusion that aging does not alter the dominant time-dependent deformation mechanism, but instead modulates the resistance to the

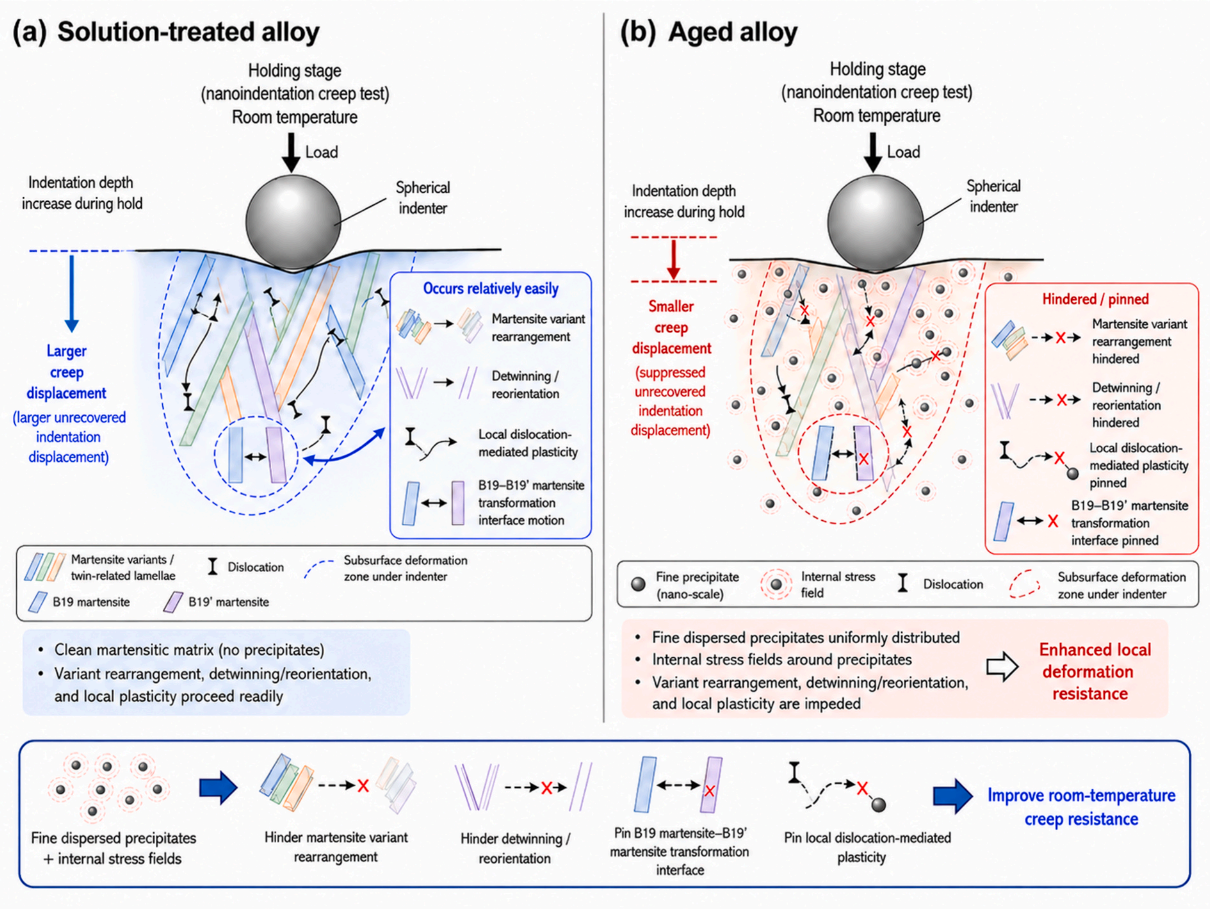

Fig. 5. Schematic illustration of the room-temperature indentation creep mechanisms in solution-treated and aged Ti-rich Ti–Ni–Cu–Pd alloys.

existing interface-mediated process through the pinning effects of finely dispersed precipitates and their associated local stress fields.

Based on the above results, a room-temperature indentation creep mechanism model can be established, as schematically illustrated in Fig. 5. For the solution-treated alloy, the region beneath the indenter consists of a relatively clean martensitic matrix, where martensite variant rearrangement, detwinning, and local dislocation-mediated plasticity can occur more readily. Consequently, during the holding stage, the indentation depth continues to increase, resulting in a larger creep displacement and a greater irreversible indentation displacement. For the aged alloy, fine dispersed precipitates are uniformly distributed within the martensitic matrix, accompanied by localized internal stress fields around them. These precipitates and their associated internal stress fields can hinder martensite variant rearrangement, suppress detwinning/reorientation processes, and pin the B19→B19’ transformation interfaces as well as local dislocation-mediated plastic deformation. As a result, the aged sample exhibits a smaller creep displacement, a lower quasi-steady-state creep strain rate, and slightly higher apparent stress exponent and activation volume under the same indentation strain or contact stress. Overall, aging treatment effectively improves the room-temperature indentation creep resistance of the Ti–Ni–Cu–Pd alloy through the interaction between fine dispersed precipitates and the martensitic matrix.

4. Conclusion

Spherical nanoindentation creep experiments demonstrate that the Ti-rich Ti–Ni–Cu–Pd alloy exhibits appreciable time-dependent plastic deformation in both solution-treated and aged states even at room temperature. However, the aged state exhibits significantly reduced creep deformation compared with the solution-treated state, indicating that the introduction of fine, dispersed precipitates effectively enhances the creep resistance of the alloy. Furthermore, analysis based on the creep stress exponent, *n*, and the corresponding activation volumes suggests that the dominant creep mechanisms are associated with localized martensitic interfacial motion rather than conventional dislocation-controlled power-law creep. The time-dependent deformation is mainly accommodated by martensite variant rearrangement, detwinning/reorientation, and local B19/B19’ transformation-interface migration, with limited dislocation slip at higher indentation strains. In the aged alloy, fine dispersed precipitates and their associated internal stress fields impede these interfacial processes and restrict local dislocation-mediated plasticity, leading to enhanced room-temperature indentation creep resistance. These findings provide useful insight into the room-temperature time-dependent deformation behavior of the Ti-rich Ti–Ni–Cu–Pd alloy and highlight the important role of aging treatment in improving its deformation resistance.

Declaration of competing interest

The authors declare that they have no known competing financial interests or personal relationships that could have appeared to influence the work reported in this paper.

Acknowledgements

The work at Shihezi University was supported in part by the Research Start-up Fund for High-level Talents of Shihezi University (No. RCZK2025111), and in part by the China Scholarship Council Visiting Scholar Program (No. 201908230066). The work at Hanyang University was supported by the National Research Foundation of Korea (NRF) grant funded by the Korea government (MSIT) (No. 2022R1A5A1030054 and RS-2026-25478573).

References

[1] Bhattacharya K, James RD. The materials is the machine. Science 2005;307:53–4. https://doi.org/10.1126/science.1100892.

[2] Miyazaki S, Ishida A. Martensitic transformation and shape memory behavior in sputter-deposited TiNi-base thin films. Mater Sci Eng 1999;273–275:106–33. https://doi.org/10.1016/S0921-5093(99)00292-0.

[3] Miyazaki S, Igo Y, Otsuka K. Effect of thermal cycling on the transformation temperatures of Ti-Ni alloys. Acta Metall 1986;34:2045–51. https://doi.org/10.1016/0001-6160(86)90263-4.

[4] Tadaki T, Nakata Y, Shimizu K. Thermal cycling effects in an aged Ni-rich Ti-Ni shape memory alloy. Trans Japan Inst Met 1987;28:883–90. https://doi.org/10.2320/matertrans1960.28.883.

[5] Pelton AR, Huang GH, Moinec P, Sinclair R. Effects of thermal cycling on microstructure and properties in nitinol. Mater Sci Eng 2012;532:130–8. https://doi.org/10.1016/j.msea.2011.10.073.

[6] Zarnetta R, Takahashi R, Young ML, et al. Identification of Quaternary shape memory alloys with near-zero thermal hysteresis and unpercedented functional stability. Adv Funct Mater 2010;20:1917–23. https://doi.org/10.1002/adfm.200902336.

[7] Li H, Meng XL, Cai W. Effects of Pd content on microstructures, martensitic transformation of $Ti_{50.5}Ni_{38\text{-}x}Cu_{11.5}Pd_x$ (x = 3, 4, 4.5, 5.5) alloys. J Alloys Compd 2019;791:905–10. https://doi.org/10.1016/j.jallcom.2019.03.372.

[8] Li H, Meng XL, Cai W. Martensitic transformation and microstructure of (Ni, Cu, Pd)-rich $Ti_{49.5}Ni_{39\text{-}x}Cu_{11.5}Pd_x$ alloys with near-zero hysteresis and excellent thermal stability. Intermetallics 2020;126:106927. https://doi.org/10.1016/j.intermet.2020.106927.

[9] Meng XL, Li H, Cai W, Hao SJ, Cui LS. Thermal cycling stability mechanism of Ti50.5Ni33.5Cu11.5Pd4.5 shape memory alloy with near-zero hysteresis. Scr Mater 2015;103:30–3. https://doi.org/10.1016/j.scriptamat.2015.02.030.

[10] Meng XL, Li H, Cai W. Effect of training on the temperature memory effect in Ti49.5Ni34.5Cu11.5Pd4.5 shape memory alloy with narrow hysteresis. Scr Mater 2016;118:29–32. https://doi.org/10.1016/j.scriptamat.2016.03.003.

[11] Li H, Meng XL, Cai W. Shape memory behaviors in a $Ti_{50}Ni_{33.5}Cu_{12.5}Pd_4$ alloy with near-zero thermal hysteresis. J Alloys Compd 2018;765:166–70. https://doi.org/10.1016/j.jallcom.2018.06.205.

[12] Eggeler G, Hornbogen E, Yawny A, Heckmann A, Wagner M. Structural and functional fatigue of NiTi shape memory alloys. Mater Sci Eng 2004;378:24–33. https://doi.org/10.1016/j.msea.2003.10.327.

[13] Frenzel J. On the importance of structural and functional fatigue in shape memory technology. Shape Memory and Superelasticity 2020;6:213–22. https://doi.org/10.1007/s40830-020-00281-3.

[14] Raj SV, Noebe RD. Low temperature creep of hot-extruded near-stoichiometric NiTi shape memory alloy part I: isothermal creep. Mater Sci Eng 2013;581:145–53. https://doi.org/10.1016/j.msea.2013.04.040.

[15] Khan MI, Kim HY, Nam T, Miyazaki S. Formation of nanoscaled precipitates and their effects on the high-temperature shape-memory characteristics of a $Ti_{50}Ni_{15}Pd_{25}Cu_{10}$ alloy. Acta Mater 2012;60:5900–13. https://doi.org/10.1016/j.actamat.2012.07.032.

[16] Khan MI, Kim HY, Namigata Y, Nam T, Miyazaki S. Combined effects of work hardening and precipitation strengthening on the cyclic stability of TiNiPdCu-based high-temperature shape memory alloys. Acta Mater 2013;61:4797–810. https://doi.org/10.1016/j.actamat.2013.04.066.

[17] Li H, Gao Z, Suh J-Y, Han HN, Ramamurty U, Jang J-i. On the superelastic behavior during spherical nanoindentation of a Ni-Ti shape memory alloy. Materialia 2024;33:102020. https://doi.org/10.1016/j.mtla.2024.102020.

[18] Li H, Gao Z, Bai XX, Jin YM, Meng XL, Cai W, Suh J-Y, Jang J-i. High-strength gradient Ti-Ni-Cu-Pd ribbon with large recoverable strain and high cyclic stability under load. Mater Res Lett 2026;14:267–75. https://doi.org/10.1080/21663831.2026.2613044.

[19] Resnina N, Belyaev S, Bazlov A, et al. Palladium-free multicomponent high temperature shape memory alloys. Int J Eng Sci 2024;197:104027. https://doi.org/10.1016/j.ijengsci.2024.104027.

[20] Li X, Bhushan B. A review of nanoindentation continuous stiffness measurement technique and its applications. Mater Charact 2002;48:11–36. https://doi.org/10.1016/S1044-5803(02)00192-4.

[21] Maier V, Merle B, Göken M, Durst K. An improved long-term nanoindentation creep testing approach for studying the local deformation processes in nanocrystalline metals at room and elevated temperatures. J Mater Res 2013;28:1177–88. https://doi.org/10.1557/jmr.2013.39.

[22] Choi IC, Yoo BG, Kim YJ, Jang J-i. Indentation creep revisited. J Mater Res 2012;27:3–11. https://doi.org/10.1557/jmr.2011.213.

[23] Yoo BG, Kim KS, Oh JH, Ramamurty U, Jang J-i. Room temperature creep in amorphous alloys: influence of initial strain and free volume. Scr Mater 2010;63:1205–8. https://doi.org/10.1016/j.scriptamat.2010.08.034.

[24] Lee DH, Seok MY, Zhao Y, Choi IC, He J, Lu Z, Suh JY, Ramamurty U, Kawasaki M, Langdon TG, Jang J-i. Spherical nanoindentation creep behavior of nanocrystalline and coarse-grained CoCrFeMnNi high-entropy alloys. Acta Mater 2016;109:314–22. https://doi.org/10.1016/j.actamat.2016.02.049.

[25] Islam MM, Bayati P, Nematollahi M, Jahadakbar A, Elahinia M, Haghshenas M. Ambient-temperature indentation creep of shape memory NiTi alloys: additively manufactured versus cast. J Manuf Mater Process 2021;5:87. https://doi.org/10.3390/jmmp5030087.

[26] Kaur N, Kaur D. Room temperature nanoindentation creep of nanograined NiTiW shape memory alloy thin films. Surf Coating Technol 2014;260:260–5. https://doi.org/10.1016/j.surfcoat.2014.07.090.

[27] Li H, Meng XL, Cai W. Microstructures, martensitic transformation and shape memory behaviors of aged $Ti_{50.5}Ni_{33.5}Cu_{11.5}Pd_{4.5}$ alloys. J Alloys Compd 2019;780:800–4. https://doi.org/10.1016/j.jallcom.2018.12.030.

[28] Meng XL, Sato M, Ishida A. Structure of martensite in deformed Ti-Ni-Cu thin films. Acta Mater 2011;59:2535–43. https://doi.org/10.1016/j.actamat.2011.01.003.

[29] Johnson KL. Contact mechanics. Cambridge: Cambridge University Press; 1985.

[30] Choi I-C, Yoo B-G, Kim Y-J, Seok M-Y, Wang YM, Jang J-i. Estimating the stress exponent of nanocrystalline nickel: sharp vs. spherical indentation. Scr Mater 2011;65:300–3. https://doi.org/10.1016/j.scriptamat.2011.04.031.

[31] Wang CL, Lai YH, Huang JC, Nieh TG. Creep of nanocrystalline nickel: a direct comparison between uniaxial and nanoindentation creep. Scr Mater 2010;62:175–8. https://doi.org/10.1016/j.scriptamat.2009.10.021.

[32] Yavari P, Langdon TG. An examination of the breakdown in creep by viscous glide in solid solution alloys at high stress levels. Acta Metall 1982;30:2181–96. https://doi.org/10.1016/0001-6160(82)90139-0.

[33] Langdon TG. Grain boundary sliding revisited: developments in sliding over four decades. J Mater Sci 2006;41:597–609. https://doi.org/10.1007/s10853-006-6476-0.

[34] Zhu T, Li J, Samanta A, Kim H-G, Suresh S. Interfacial plasticity governs strain rate sensitivity and ductility in nanostructured metals. Proc Natl Acad Sci U S A 2007;104:3031–6. https://doi.org/10.1073/pnas.0611097104.

[35] Frost HJ, Ashby MF. Deformation-Mechanism maps: the plasticity and creep of metals and ceramics. Oxford: Pergamon Press; 1982.

[36] Conrad H. Plastic deformation kinetics in nanocrystalline FCC metals based on the pile-up of dislocations. Nanotechnology 2007;18:325701. https://doi.org/10.1088/0957-4484/18/32/325701.